Design of an Atomic Layer Deposition System with *in situ* Reflection High Energy Electron Diffraction

Alexandra J. Howzen[1], Justin Caspar[2], Dr. Alparslan Oztekin[2], and Dr. Nicholas C. Strandwitz[1]

[1] Department of Materials Science and Engineering, Lehigh University, Bethlehem, Pennsylvania 18015, United States
[2] Department of Mechanical Engineering and Mechanics, Lehigh University, Bethlehem, Pennsylvania 18015, United States

The author to whom correspondence may be addressed: nis212@lehigh.edu

Abstract

We report the design, fabrication, and testing of an atomic layer deposition (ALD) system that is capable of reflection high energy electron diffraction (RHEED) in a single chamber. The details and specifications of the system are described and include capabilities of RHEED at varied accelerating voltages, sample rotation (azimuthal) control, sample height control, sample heating up to set temperatures of 1050 °C, and either single- or dual-differential pumping designs. Thermal and flow simulations were used to justify selected system dimensions as well as carrier gas/precursor mass flow rates. Temperature calibration was conducted to determine actual sample temperatures that are necessary for meaningful analysis of thermally-induced transitions in ALD thin films. Several demonstrations of RHEED in the system are described. Calibration of the camera length was conducted using a gold thin film by analyzing RHEED images. Finally, RHEED conducted at a series of increasing temperatures was used to monitor the crystallization of an ALD HfO_2 thin film. The crystallization temperature and the ring pattern was consistent with the monoclinic structure as determined by separate XRD-based measurements.

I. Introduction

Atomic layer deposition (ALD) utilizes sequential, self-limiting chemical reactions between vapor precursors and a surface that result in film growth[1]. ALD allows for the deposition of a wide range of material compositions and boasts sub-nanometer thickness control and conformal growth even on high

aspect ratio, non-planar, or porous substrates[2,3]. ALD film growth typically occurs within a temperature window (commonly referred to as the "ALD window") that defines the range over which growth is self-limiting. At low temperatures, precursor condensation and/or slow surface reactions can yield non-uniform or no growth. At high temperatures, precursor decomposition and/or surface desorption can occur. For many film chemistries, the maximum temperature of the ALD window is dictated by precursor decomposition and is often too low to create crystalline films or achieve epitaxial growth[4]. Examples of exceptions to this observation include ZnO and MgO, for which crystalline films can be grown directly within the ALD window[4].

When the ALD window precludes direct growth of crystalline phases, thermal processing can be utilized between ALD cycles to bypass the effects of precursor decomposition at temperatures above the ALD window. In principle, this thermal cycling may allow for the growth of crystalline or epitaxial films via ALD in cases where the precursor decomposition would prevent the use of high growth temperatures. Previous work studying the effects of *in situ* annealing between ALD cycles include the intermittent annealing of amorphous HfO_2 and $HfAlO_x$[5–9]; the decomposition of trimethylaluminum (TMA) through flash lamp annealing to produce metallic Al films[10–12]; and the use of pulse heating ALD to produce high quality, epitaxial ZnO films vs the polycrystalline films typically grown via traditional thermal ALD[13]. Using intermittent annealing between ALD cycles produced oxide films with increased density relative to films deposited without the additional thermal cycling and similar to those seen in films deposited at higher temperatures or given a single post-deposition anneal[8–10]. Although this strategy shows promise, details of the structural changes that occur during annealing are challenging to access and would require *in situ* structural analysis.

Various techniques have been utilized for *in situ* structural analysis during deposition such as X-ray scattering[14–17], X-ray diffraction[18,19], and X-ray reflectivity[20–22]. These techniques are readily compatible with ALD due to the use of X-ray photons, which interact weakly with gas molecules. Prior

in situ X-ray-based studies of film growth emphasize the importance of studying initial film nucleation and coalescence, and how that influences the resulting film properties[15,17–19,23,24]. However, the small thicknesses associated with the initial stages of ALD film growth and the small absorption/scattering cross section of X-ray photons generally require ultra-bright synchrotron radiation sources that still present challenges to probing the film structure.

In contrast, electron diffraction techniques, such as reflection high energy electron diffraction (RHEED) and low energy electron diffraction (LEED), are useful for monitoring the structure of surfaces and ultrathin films. RHEED is widely utilized in molecular beam epitaxy (MBE) and pulsed laser deposition (PLD) systems to monitor initial film growth and structure[25–28]. A key drawback of electron diffraction techniques is the interaction of electrons with gas molecules and is particularly relevant to ALD due to high growth pressures (~1×10^{-2} to 1×10^{-1} Torr) typically used relative to PLD (1×10^{-4} to 1×10^{-2} Torr) and MBE (1×10^{-7} Torr). The impacts of this electron interaction with gas species can be minimized by pumping the system to lower pressures between ALD precursor exposures or by minimizing the electron path length within the high-pressure environment.

Some precedent exists demonstrating the value of RHEED in the analysis of ALD films and surfaces. The technique has been used to determine the crystallization temperature of amorphous films by acquiring RHEED patterns as a function of temperature during an anneal[29]. RHEED has been used to determine the crystal quality of films and to monitor increases in surface order after annealing by evaluating the presence and intensity of streaky RHEED patterns[30,31]. Prior studies have also utilized RHEED to evaluate whether deposited films are epitaxial and determine their structure and epitaxial relationship to the substrate[30,32,33]. Since RHEED is primarily sensitive to the first few atomic layers, it can also be used to determine the surface reconstructions of crystalline buffer layers and their subsequent impact on additional film deposition[28]. Recent work has also shown that RHEED can observe the epitaxial crystallization of both thin seed layers and thicker amorphous films[34]. Although RHEED has demonstrated

the ability to determine minute changes in surface structure when depositing or annealing ALD films, much of the prior work has been conducted by film transfer from an ALD chamber to a high vacuum chamber (such as an MBE chamber) so RHEED can be performed.

Very few studies have described the limitations, design, and demonstration of a system capable of conducting RHEED within an ALD system without requiring sample transfer[35,36]. In seminal work on this topic, Bankras et al described a RHEED-capable ALD system that consisted of a self-contained, heated cylinder with two slits that allowed the RHEED beam to enter and exit the deposition/substrate area. This deposition chamber was situated inside of a larger ultra-high vacuum chamber that reduced the interaction of the beam in the relatively high-pressure film growth zone to minimize electron scattering.This custom system was used to continuously monitor a TMA/water growth chemistry resulting in the deposition of aluminum oxide on silicon. A gradual decrease in the diffraction intensity from the Si substrate with increasing number of ALD cycles was observed. Additionally, a difference in the RHEED intensity for TMA- vs water-terminated surfaces was also observed and attributed to different scattering properties between the two terminations[36]. One limitation of this design is the use of small slits when the electron beam enters the deposition area to minimize pressure rises, which limits the angular range of incident and diffracted/reflected electron beam, thus making advanced analysis using rocking curves difficult and cuts off portions of accessible reciprocal space[37]. Further, rotational (azimuthal) scanning and RHEED rocking curve acquisition were likely not possible in this system.

This work describes the design, construction, and demonstration of a RHEED-capable ALD system that allows for structural monitoring during film growth with access to substrate rotation and a wide range of incident/diffracted electron beam angles. The design requirements for developing a chamber capable of incorporating traditional high vacuum RHEED or differentially pumped RHEED under reactive gasses are outlined. Finally, system calibration is demonstrated and the ability to perform *in situ* structural analysis with RHEED is shown by observing the crystallization of a hafnium oxide film upon heating.

II. Instrument Description

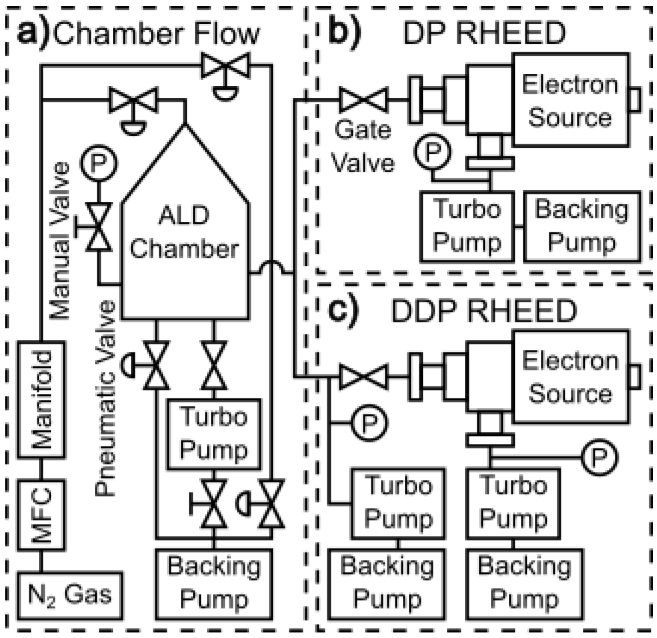

Figure 1: Gas flow diagram of the a) ALD component of the system that can be equipped with either b) a single differentially pumped RHEED or c) a dual differentially pumped RHEED system.

The *in situ* RHEED ALD chamber was designed with two possible configurations for RHEED integration (**Figure 1**). The ALD components of the overall system (**Figure 1a**) will be discussed first and are largely independent of the two RHEED configurations. First, research-grade (99.9999%) N_2 is supplied to a mass flow controller (MFC) with a maximum flow rate of 500 sccm through a 1/4-inch stainless steel line (model numbers for components are listed in Supplemental Table 1). The gas then flows through the precursor manifold, which can accommodate a maximum of four precursors that are separated from the carrier gas flow line by a manual valve followed by fast-switching, pneumatically-actuated ALD valves. All carrier gas lines and system components that contain precursor vapors are heated from the precursor manifold, through the sample chamber, and up to the system pumps to prevent the condensation of precursor vapors. The ALD precursors are introduced via vapor draw into the system. After the

manifold, the heated carrier gas line is split two ways by using a T-shaped monoblock manifold with two ALD diaphragm valves. One path directs the gas flow to a conical inlet that connects to the top of the cylindrical growth chamber, while the second directs the gas flow to a bypass line that feeds directly into a dry scroll pump (max pumping speed of 1.7 L/s). The valves that separate the roughing pump from the chamber only activate as open/closed and have no ability for variable conductance. As the outlet pumping speed is constant regardless of the inlet flow rate through the MFC, varying the inlet flow rate also controls the chamber pressure. The conical inlet and cylindrical growth chamber were designed in-house using SolidWorks and fabricated by the Kurt J. Lesker Company from 304L stainless steel; due to its corrosion resistance, smooth surface finish when polished, and reduced magnetic fields relative to other stainless steels.

The chamber is heated, beginning at the inlet and ending at the chamber bottom. The precursor manifold is heated using two cylindrical cartridge heaters inserted into a custom, hollow aluminum clamshell. The chamber inlet line and body are heated with 0.5 in wide, medium-watt density heating tape. The sample is heated using a 2 in diameter stage that can reach a maximum set temperature of 1050 °C. The stage is positioned face-up and is capable of 360° azimuthal rotation and z-height manipulation of 1 in above and below the beam centerline for a full range of 2 in. The lowest stage position is 0 in, and produces the largest incident angle for RHEED analysis. The stage is designed for use in PLD and is tolerant of reactive gasses such as oxygen even at high stage temperatures and partial pressures approaching 1 atm.

The chamber body is equipped with conflat (CF) ports for a door for sample loading/unloading, the RHEED electron source and screen, and four auxiliary connections. The door is mounted on an 8 in outer diameter (OD) CF and has a 5.5 in OD leaded glass window. The door is sealed via a compression seal with a Kalrez o-ring which has a maximum operating temperature of 250 °C. Two potential chamber diameters of 8 and 10 inches were examined in simulations because they corresponded to the standard

inner diameter for 10 and 12 in OD CF flanges. The smaller chamber diameter would allow for shorter purge times, but a larger chamber diameter would give more distance between the heated sample stage and the chamber door and resulting in a lower temperature at the Kalrez o-ring. Based on these simulations (discussed below), the 10 in cylinder diameter with 12 in OD CF end connections was chosen for the chamber body due to the temperature constraint.

The conical inlet that sits on top of the chamber body has a 2.75 in OD CF at the top (inlet) and 12 in OD CF at the bottom (outlet to cylindrical chamber) with a body slope of 30° from the centerline. The sample stage sits on a 12 in CF blank with two 4.5 in OD CF outlet lines angled 30° off of the vertical centerline. The first line is equipped with an adapter that connects to a QF 25 pneumatic "stop" valve that connects directly to the chamber scroll pump for use during deposition. The second line has an adapter that connects the chamber to a 6 in OD CF, pneumatically controlled UHV gate valve that is attached to a 6 in OD CF inlet turbomolecular pump (maximum pumping speed of 345 L/s for nitrogen gas). The turbo pump backing line is connected to a QF 25 manual valve that allows the turbo pump to be isolated from the chamber and pumping line during deposition. The manual valve is attached to the chamber scroll pump and allows this pump to back the turbopump. The bypass line also has a pneumatic ALD valve at the bottom connection to the pump so that the entire bypass line does not need to be actively pumped when not in use. Photographs of the system can be seen in Supplemental Figure 1.

A schematic of the system for the two different RHEED integration configurations includes differentially pumped (DP) and dual differentially pumped (DDP) options (Figures 1, 2). Note that the schematic in Figure 2 shows only the chamber inlet, chamber, RHEED screen, RHEED gun region, and chamber outlet; and omits the manifold, manifold-to-inlet line, bypass line, and pumping lines for clarity. We note that in this work, we have not experimentally demonstrated the DDP configuration (Figure 1c, 2b) due to time and financial constraints, but we have described it sufficiently such that it could be implemented on this system or a similar reproduction. Justification for the selected system specifications

and the DP and DDP configurations is described below in Section II, but the physical description of these configurations is as follows.

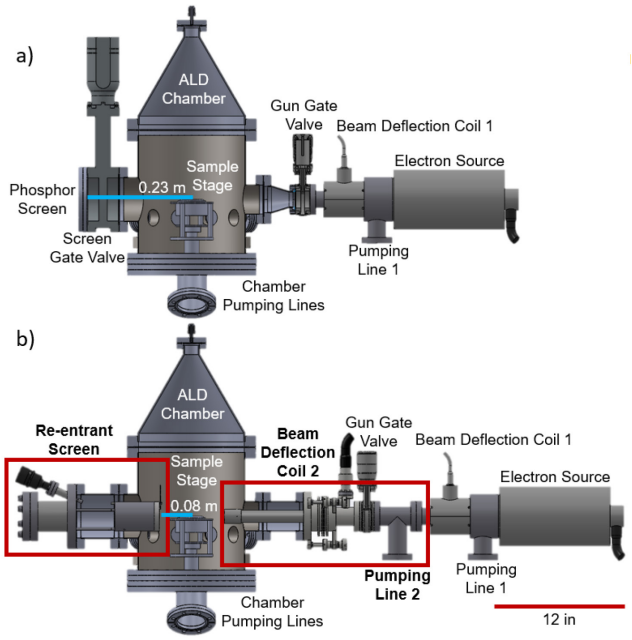

Figure 2: Schematic of the chamber for a) differentially pumped (DP) RHEED and b) dual differentially pumped (DDP) RHEED chamber configurations. The red boxes highlight the additions that need to be made to the DP configuration to achieve the DDP configuration. The blue lines indicate the camera length, the length between the center of the sample stage and the phosphor screen, for the DP and DDP configurations.

In the differentially pumped (DP) configuration, the electron source is connected directly to the 2.75 in OD CF pneumatic gate valve. The electron source has an internal orifice that permits up to a three-order-of-magnitude difference in pressure between the main chamber and electron source. Therefore, "Pumping Line 1" is connected to a turbopump and scroll backing pump that is only dedicated to the electron gun region. Copper magnetic deflection coils are located between the electron source and the gate valve and control the x and y beam deflections, which are used to adjust the beam position on the sample and the beam rocking parameter, which expands the range of incident angles. A 2.75 in OD to 4.5 in OD

conical adapter connects the gate valve to the 4.5 in OD CF chamber port. The leaded phosphor screen that displays the RHEED pattern is inset into a blank 6 in OD CF with a leaded glass window opposite the electron gun and is viewed from outside the chamber by a light-enclosed, monochromatic, CMOS camera. The camera enclosure is an accordion flange mount that attaches to the 6 in blank via external set screws. The 6 in phosphor screen is connected to a pneumatically-controlled gate valve, which is attached to the chamber body. The electron source and screen CF flanges are parallel and concentric such that an undeflected electron beam will fall on the center of the screen (**Figure 2a**).

The pneumatic gate valves installed between the chamber and the RHEED electron source and between the chamber and the phosphor screen in the DP configuration can isolate these components during deposition. By closing the stop valve, opening the gate and manual valves on the turbo pumping line, and diverting the carrier gas through the bypass line; the chamber can be pumped down to high vacuum with the turbo pump. The bypass line allows for less than 20 sccm of continuous nitrogen flow through the rest of the system, including the precursor manifold when the chamber is under UHV in order to maintain proper backing pressure for the turbo pump. This constraint could be removed by implementing two, separate roughing pumps for the bypass and the turbo backing lines. Nonetheless, the current configuration allows switching between low and high vacuum conditions without a throttle valve, and allows for ALD growth without flowing precursor vapor through the turbo pump.

The dual differentially pumped (DDP) configuration has several differences from the DP configuration highlighted in the red rectangles in Figure 2b. A second pumping line is inserted between the gun gate valve and the chamber flange. This pumping line and a second orifice at the end of the DDP reentrant beam nozzle create three independently pumped pressure zones for a total maximum of six orders of magnitude pressure difference between the electron source and chamber. Due to the now increased path length within the gun assembly, a second deflection coil setup is added to the reentrant beam nozzle for additional x and y deflection control. The DDP configuration also has a 2 in diameter screen that is

reentrant into the chamber that can no longer be protected by a gate valve, which is omitted in this configuration (left red box, Figure 2b). The reentrant electron source and screen decrease the electron path length from 21 in or 0.53 m (DP) to 6 in or 0.15 m (DDP). The reentrant screen and electron gun are the only differences between the DP and DDP configurations in the ALD-portion (**Figure 1a**) of the instrument. Although the DDP configuration is not experimentally verified in this work, the hardware needed to implement this configuration is identified and is commercially available.

A custom Python program is used to control the deposition and analysis processes. All ALD valves for the precursor pulsing and bypass line, gate valves, and stop valve are controlled via a digital signal from a National Instruments (NI) board and are all pneumatically actuated. The chamber and inlet heating tapes are controlled by the same Python program via RS-485 communication with temperature/process controllers. Similarly, all stage heating and motor components are controlled using proprietary software from the stage manufacturer (Neocera), all RHEED controls can be actuated using analog outputs from Python, and camera image capturing is controlled using Vimba Viewer, a proprietary software for Allied Vision cameras.

II. RHEED Incorporation and Operation

Several factors were considered when implementing RHEED in ALD, most notably 1) protecting the electron gun filament and 2) managing electron scattering off gas molecules. These two factors are addressed in succession below.

Differential pumping protects the electron source filament even while the chamber is at pressures above UHV conditions. For example, to sustain a typical current of 1.5 μA on the filament without causing failure, the pressure in the electron source should not exceed 5×10^{-6} Torr. For a DP configuration, this constraint means that the pressure within the chamber can be as high as 5×10^{-3} Torr without damaging the RHEED filament. The second differential pumping line introduced in the DDP setup allows the chamber

pressure to be increased to approximately 0.5 Torr which is above the typical ALD process pressure of 0.1 Torr. Therefore, in this DDP configuration, real time structural analysis can be conducted during sequential chemical vapor exposures that constitute ALD at typical ALD pressures, rather than between ALD exposures coupled with pump-downs to lower pressure.

After accounting for the above constraints on pressure to protect the electron source filament, electron scattering must be considered in order to minimize gas scattering of the electron beam, which can cause blurring or complete loss of RHEED images. The mean free path of an electron can be used as a simple metric to assess scattering from vapor/gas species[38]:

$$\lambda_{MFP} = \frac{R * T}{P * \sigma * N_A\sqrt{2}} \quad (1)$$

where λ_{MFP} is the mean free path in m (MFP), R is the universal gas constant in m^3*Torr/K*mol, T is the temperature in K, P is the chamber pressure in Torr, σ is the collision cross-section of the purging gas atom in m^2 (in this case σ for nitrogen is 0.43 nm^2), and N_A is Avogadro's number in atoms/mol. The calculated λ_{MFP} was compared to the total distance the electrons must travel through the chamber to the screen (21 in or 0.53 m for the DP configuration). Here, we assign the maximum chamber pressure that can permit RHEED analysis as the pressure at which λ_{MFP} is equal to the physical dimensions of 21 in (0.53 m). This assignment is arbitrary, because there is no specific cutoff in the amount of scattering that can be tolerated. This assignment is depicted by the intersection of the horizontal lines (the physical path length of an electron for the DP or DDP configurations) and the solid or dotted slanted lines in Figure 3. For nitrogen gas at 850 °C, the maximum pressure is approximately $1x10^{-3}$ Torr, and is below the typical pressure for ALD of approximately 0.1 Torr. This pressure constraint requires that either 1) lower than typical pressures be used for precursor exposure and purging steps or 2) the chamber pressure be decreased *between* ALD cycles to allow for RHEED analysis in the DP configuration without significant electron

scattering. Our studies and experimental demonstrations have focused on the latter option. Thus, the chamber should be capable of attaining both low (>1x10^{-3} Torr) and high (<1x10^{-3} Torr) vacuum conditions for deposition and analysis respectively.

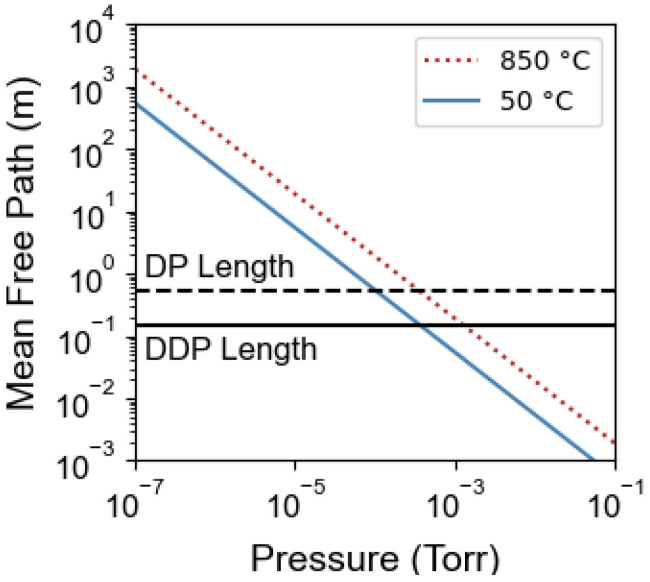

Figure 3: Calculated mean free path of an electron in N_2 at 50 and 850 °C along with two horizontal lines representing the physical distance between where the electron beam enters the chamber and the RHEED screen surface for the DP configuration (21 in, 0.53 m) dashed line and DDP configuration (6 in, 0.15 m) solid line.

There are benefits and drawbacks for both configurations of the RHEED system. For the DP configuration, drawbacks include 1) the inability to measure RHEED during precursor exposure steps and relatedly, 2) the necessity to pump down the main chamber after precursor exposure steps prior to RHEED imaging. Advantages of the DP configuration include 1) the electron gun and screen are protected via the use of gate valves during precursor exposure steps, 2) long scattering (camera) lengths relative to the DDP configuration, and 3) minimized electron scattering by operation at low pressures. Item 2) is an advantage because the long scattering length results in greater physical separation between illuminated features on the phosphor screen. Conversely, disadvantages of the DDP configuration include loss of sharpness in the

RHEED patterns via electron-gas scattering, 2) decreased camera length and subsequent decreased separation of diffraction features, 3) decreased (reentrant) screen size, which is farther away from the viewport and camera than in the DP configuration, and 4) lack of protection for the screen from chemical vapor exposures due to the lack of gate valves.

V. Simulating Stage Heat Radiation and Chamber Gas Flow

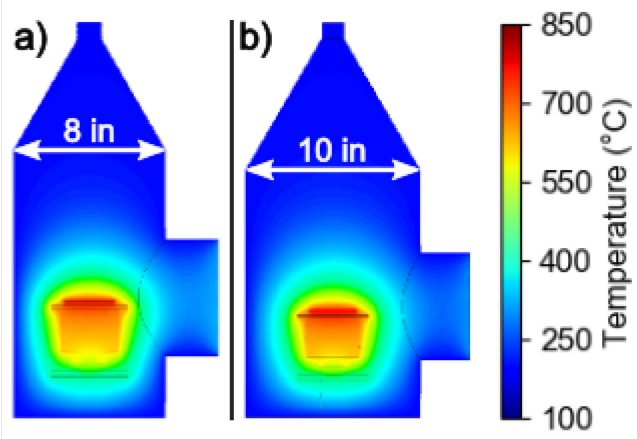

Figure 4: Simulated radiative heating caused by the stage at 850 °C and the chamber walls are at 100 °C for consideration of a) the design with an 8 in chamber diameter and b) the design with a 10 in chamber diameter.

Two simulations were conducted to provide further details of the heat transfer and gas flow inside the ALD chamber. The flow simulations within the chamber were conducted using computational fluid dynamics (CFD) software (Ansys-Fluent 19.1). For incompressible Newtonian fluids, the Navier-Stokes equations (the conservation of mass and momentum) are used to describe the flow. For the heat transfer simulations, the energy equation with radiation terms present is considered to govern heat transfer within the channel. The Fluent Surface-to-Surface model is used to calculate view factors. By conducting simulations, the aim is to help to optimize designs, assess performance, and make informed decisions about chamber design and process parameters.

First, a radiation heat transfer model was used to choose a chamber diameter to keep the chamber door's Kalrez o-ring lower than 250 °C during operation. High vacuum heat transfer simulations were conducted with the stage at its maximum expected sample face temperature of 850 °C. The stage face was treated as the heat source, and the walls were held at 100 °C with an absorptivity near unity and with two potential chamber inner diameters of 8 and 10 inches. The 10 in chamber diameter was chosen since the door would be approximately 150-225 °C instead of the 180-260 °C temperature estimation for the 8 in diameter chamber (Figure 4).

Second, steady-state flow simulations of N_2 were also conducted for the chosen 10 in diameter chamber. Simulations of precursor flow were not included because they are expected to be dilute in the N_2 carrier gas stream. Four different flow gas flow rates (50-200 sccm) were considered as realistic operational regimes. The Knudsen number was calculated using Equation 2:

$$Kn = \frac{\lambda_{MFP}}{D_C} \tag{2}$$

where D_c is the characteristic length (chamber inner diameter, 10 inches or 0.25 meters) in meters and the λ_{MFP} is the mean free path of nitrogen gas in meters calculated using Equation 1. P and T were kept constant at 0.2 Torr and 150 °C respectively. These conditions were chosen because they represent typical deposition pressure and temperature for ALD systems. Calculating the Knudsen number is integral to properly setting the initial conditions of the flow simulation. The Knudsen number itself relates to setting the boundary, or no-slip condition between the fluid and the chamber walls. In order to ensure unhindered precursor delivery from the manifold, to the chamber, and ultimately to the substrate on the sample stage; the system should be in laminar flow which is present for a low Reynold's number. The Knudsen number was calculated to be 0.0014 with these parameters. The maximum operational temperature attainable by the stage body is 1050 °C which produces a maximum Knudsen number of

0.003 at a pressure of 0.2 Torr which is still below the 0.01 requirement to maintain viscous flow within the reactor[39]. This maximum temperature was chosen as an upper limit, although it is not the typical operational temperature of the system. Due to the chamber's size, it is desirable to use the greatest possible inlet flow rate while maintaining laminar flow throughout the chamber to decrease the overall purge time required to prevent precursors from interacting in the vapor phase. Since P is in the denominator of Equation 1, increasing the inlet flow rate will decrease the Knudsen number and the flow through the chamber will remain in the viscous flow regime regardless of the increase.

The emergence of vortices at higher flow rates may occur and was simulated by varying the mass flow rate through the system (Figure 5). The kinematic viscosity (ν) of nitrogen was calculated to be $2x10^{-5}$ m^2/s by dividing the dynamic viscosity calculated using Sutherland's law of viscosity by the density. A no-slip, no-penetration boundary condition was applied to the chamber walls. A 0.125 in gas inlet diameter was used, with flow rates ranging from 50 to 200 sccm which has a corresponding inlet velocity: V_{inlet}. Reynolds numbers ($Re = V_{inlet} D / \nu$) between 7.5 and 31 were determined using the inlet mass flow rates and the inlet tube diameter, D (10 in or 0.25 m, as the characteristic length. The outlet was held at a constant pressure of 0.2 Torr (26.6 Pa), and a 750,000-element structured mesh was used to discretize the computational domain.

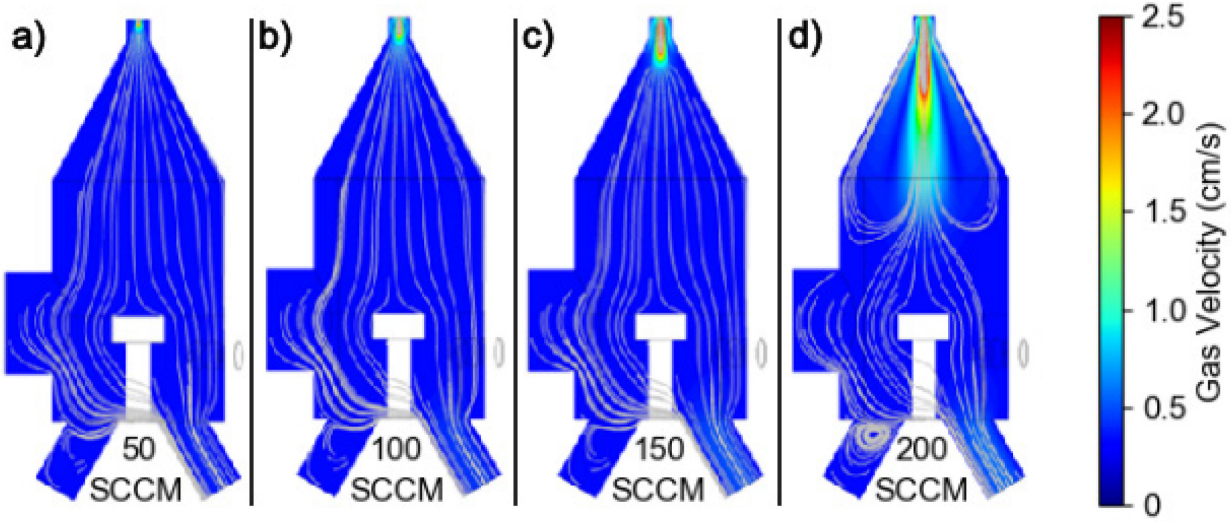

Figure 5: Simulated velocity within the chamber at an inlet velocity of a) 50, b) 100, c) 150, and d) 200 SCCM.

The gas experiences rapid expansion as it enters the chamber through a 0.125 in diameter tube at the top of the conical inlet. A conical inlet was selected to gradually increase the diameter of the region where gas/precursors are flowing until it is large enough accommodate the other system constraints (i.e., large sample holder, gate valves, etc). An abrupt change in diameter, such as going from a ¼ in gas delivery line to the 10 in chamber would likely cause dead spots in terms of gas flow, which would then result in CVD-like behavior. A vortex is formed in the conical inlet at 200 sccm which is the highest simulated flow rate (Figure 5d). Therefore, the inlet flow rates used for deposition should remain less than 150 sccm, since the simulation implies that there is no recirculation at the entrance at that inlet flow rate (see Figure 5c). Flow rates below 200 sccm show similar flow profiles. In operation, one leg of the chamber will be open, and the opposite will be closed. That is reflected by choosing only the right leg as the outlet in the chamber flow model. As the inlet flow rate increases, a vortex forms in the closed-off leg due to the change in geometry as long as the operational Reynolds number is high enough. In reality, this segment leads to the turbo pump, where the gate valve is closed to protect the pump during deposition. For future studies, a separate purge gas line between the chamber and the gate valve could improve flow during deposition. This simulation provides vital information to guide the parameters during the initial depositions.

The simulations rely on the accuracy of the given initial conditions. A potential source of error when performing CFD is using an incorrect inlet condition. The carrier gas is expected to have a fully developed flow at the chamber inlet due to the long distance the gas must travel from the source to the chamber. However, this model treats the inlet as uniform (plug) flow. This means that the chamber inlet

gas should have a parabolic velocity profile not accounted for in the model. This can lead the model to overestimate the size of any recirculation vortices created at the inlet.

VI. System Calibration

Two primary parameters are vital for quantitative structural characterization with RHEED: the camera length and beam incident angle. The camera length is the distance between where the electron beam contacts the sample and the phosphor screen. In order to measure this length without simply relying on the known physical dimensions of the system, a standard sample with a known crystal structure and composition is used[40]. The standard sample was a 90 nm thick electron-beam evaporated gold film with a 10 nm evaporated titanium metal adhesion layer on a (100) Si wafer. The RHEED pattern for the twinned, (111) oriented FCC gold structure is seen in Figure 6 for an electron accelerating voltage of 30 keV and a stage height of 0 mm (lowest height setting)[41]. The camera length (L) can be calculated using an image from a known structure:

$$L = \frac{a_{Au} * R_{(hkl)}}{\lambda_{30}\sqrt{h^2 + k^2 + l^2}} \quad (3)$$

Where h, k, and l are the miller indices of the indexed spot, R_{hkl} is the distance of the indexed spot from the direct beam spot in Å, λ_{30} is 0.07 Å or the wavelength of the electron beam at 30 keV, and a_{Au} is 4.08 Å which is the lattice parameter of FCC gold. The R_{hkl} is measured in pixels from the RHEED image, and then converted to angstroms using a constant calibrated for this specific system to be used in Equation 3.

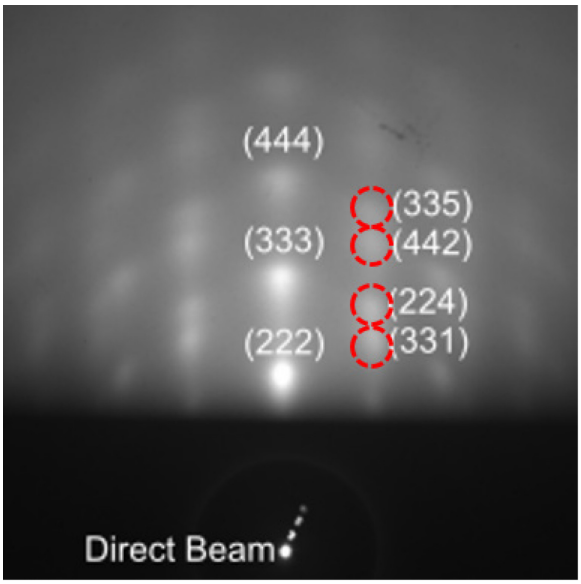

Figure 6: RHEED image of an evaporated polycrystalline gold film showing the (111)-oriented surface for the lowest stage height (0 in) which corresponds to the largest incident angle.

The camera length is constant as a function of stage height as long as the beam is at the same position on the sample. To ensure the accuracy of the calculated camera length, a series of 11 RHEED images were taken using the gold thin film standard at stage heights of 0-0.4 in where 0 is the lowest possible stage height (maximum incident angle). The camera length was calculated using the 11 most well-defined RHEED spots at each stage height and are identified in Figure 6. The average camera lengths were calculated to get the approximate camera length of 8.8 in (0.22 m). The result agrees well with the length estimated from the physical design of the system (via Solidworks drawing of the system design) of 8.9 in (0.23 m).

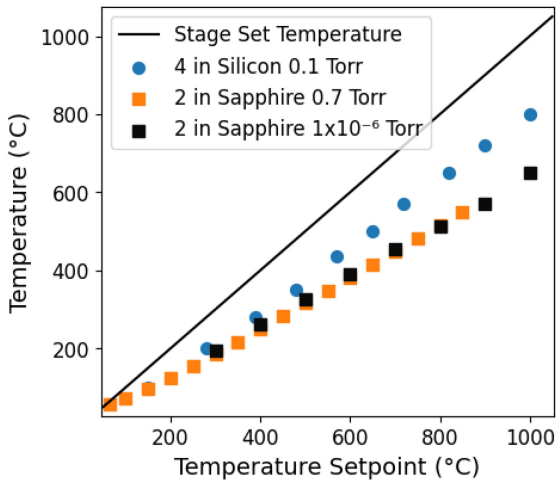

Figure 7: Temperature measured at the sample surface for a 2 in sapphire wafer at 0.7 and $1x10^{-6}$ Torr (squares) and for a calibration from the stage vendor for a larger stage (4 in stage, circles) as a function of setpoint temperature. For the 2 in sapphire measurements, a K-type thermocouple was bonded to the sapphire wafer surface using silver paste.

Wafer surface temperature is vital for understanding of the thermally-induced changes in ALD films. Therefore, calibration of the sample surface temperature for both low vacuum (0.7 Torr) and high vacuum ($1x10^{-6}$ Torr) conditions was conducted (**Figure 7**). Our sample surface temperature was measured by embedding thermocouples in silver paste (SPI Supplies 05002-AB), and similar results to those in Figure 7 were obtained when surface temperature was measured on a silicon wafer.. Wafer surface temperature was measured from 50 – 1050 °C in steps of 50 °C with a soak time of 5 minutes at each step to stabilize the temperature. The difference between the stage set temperature and the wafer surface temperature was measured at various stage set temperatures and compared to a calibration curve for a 4 in wafer (silicon) Neocera had measured for a similar model. We found that our system with a 2 in sapphire wafer differed from the set temperature by 375 °C. This number was obtained by subtracting the maximum experimentally observed temperature of 675 °C from the maximum stage set temperature of 1050 °C . Our calibration results may differ from that provided by the stage manufacturer due to a few factors: the

larger stage size used for their calibration (4 in vs. 2 in), the use of a sapphire wafer vs. a silicon wafer, and using a thermocouple attached by silver paste vs internally secured thermocouple leads. Regardless, this calibration allowed for accurate deposition and annealing temperatures to be known instead of estimating from a set temperature.

VII. Crystallization of a Hafnium Oxide ALD Film

To test the capabilities of the system, we studied the thermally induced changes of an amorphous hafnium oxide film. A 30 nm thick hafnia film was deposited on a Si wafer at 250 °C using tetrakis dimethylamido hafnium (TDMAH) and water. The resulting amorphous film was then pumped down to $7x10^{-8}$ Torr in the RHEED electron gun region and $6x10^{-6}$ Torr in the main chamber.

The RHEED source was held at an accelerating voltage of 30 keV, a filament current of 1.55 μA, and an emission current between -0.2 and -0.4 μA. The conical inlet and chamber walls were held at 120 °C and the stage set temperature was increased from 100 – 1050 °C. This corresponds to a wafer surface temperature of 65 – 675 °C and all subsequent temperature values given will be in terms of *expected wafer surface temperature* based on our prior calibration (Figure 7). In an *in situ* x-ray diffraction (XRD) study previously conducted by our group, 30 nm films deposited at 250 °C using TDMAH and water precursors crystallized into a nanocrystalline, monoclinic phase at 400 °C during a post deposition anneal in air. Changes indicative of crystallization occurred in our system at an estimated sample temperature of 415 °C (set temperature of 650 °C), only slightly different than the sample crystallized in the XRD experiment. Other sources note crystallization temperatures that vary between 200 and 500 °C[42–45]. Factors that may have contributed to the apparent difference in crystallization temperature include differences in film thickness, ambient environment, and actual temperature of the samples across the two studies. Nonetheless, the similarity in the crystallization temperatures indicates that our system calibration is likely accurate.

RHEED images initially showed no features, which is consistent with the amorphous structure of the film and can be seen in Supplemental Figure 2a. Images acquired around the crystallization temperature show the emergence of faint rings consistent with the formation of nanocrystalline domains of HfO_2. To more clearly demonstrate the presence of crystallized domains implied from the weak diffraction rings, the RHEED images were radially integrated about the direct beam spot. The result of these integrations for the image acquired at 65 °C before and after heating to 675 °C are presented along with their second derivative (**Figure 8**), and the x-axis is reported as $Å^{-1}$. The second derivative of the radially integrated images demonstrates the emergence of structure (as negative peaks) in the intensity profile of RHEED images acquired after heating at 65 °C and consistent with crystallization. The intensity profiles and second derivatives for all the acquired images are shown in Supplemental Figure 4, where a transition in the intensity profile can be observed near the proposed crystallization temperature of 415 °C.

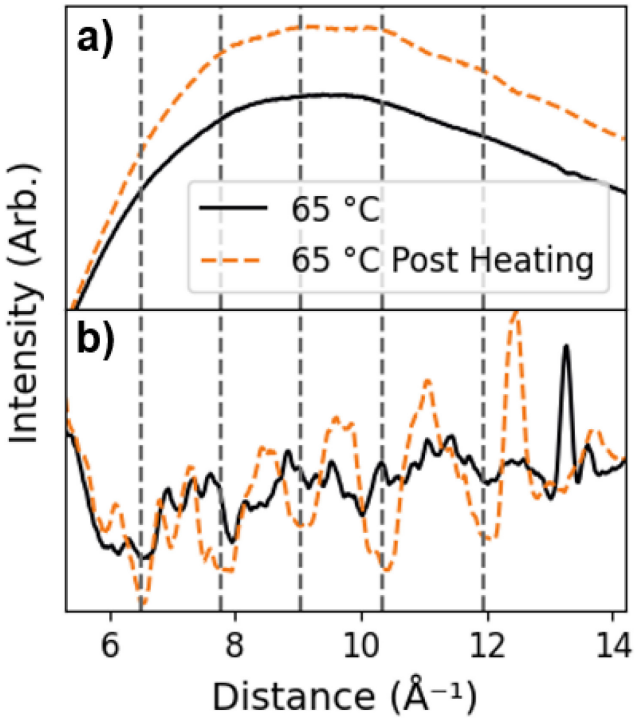

Figure 8: Radially integrated intensity of the RHEED images (a) and their second derivatives (b) acquired at 65 °C before (solid black line) and after (dashed orange line) heating to 675 °C.

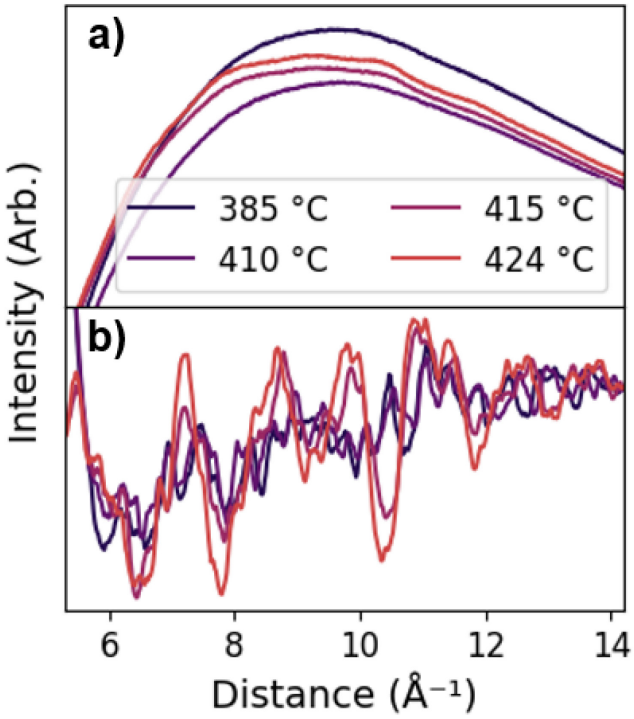

Figure 9: Plots of (a) the radially integrated intensity from RHEED images near the proposed crystallization temperature for 30 nm hafnia films and (b) the second derivative of these data.

To determine the temperature at which the crystallization began and further demonstrate the emergence of structural change around this proposed crystallization temperature, the RHEED patterns near this temperature were more closely analyzed. The raw RHEED patterns can be seen in Supplemental Figure 2. The observed halo becomes brighter until clear rings appear at 424 °C (**Supplemental Figure 2d**). To more accurately determine the restructuring temperature, the RHEED patterns were radially integrated (an explanation of radial integration can be observed in Supplemental Figure 3). There is a distinct change in the second derivative of the radially-integrated intensity between 410 and 415 °C (**Figure 9**). This change is expected since this was also near the estimated crystallization temperature for hafnia films deposited at the same temperature, with the same ALD precursors, and similar film thickness in prior work in our laboratory. A complete temperature series of the radially integrated RHEED patterns from 65 – 675 °C and 65 °C post heating can be seen in Supplemental Figure 4. The ramp rate during

annealing was 10 °C/min to increase the set temperature by 10 °C. The ramp rate increase coupled with the time to capture a RHEED pattern was approximately 6 min. This means that approximately 12 min elapsed between taking the measurement at 410 °C and 424 °C. The total time to heat from 65 to 675 °C was 4 hours and the total time to cool back to room temperature was also approximately 4 hours. Factors such as if nitrogen was flowing through the chamber and at what flow rate also impacted the cooling rate when near room temperature.

One prior publication has reported the crystallization of amorphous Al-doped HfO_2 using RHEED. That work investigated the crystallization temperature of an approximately 3.1 nm thick Al-doped HfO_2 ALD film on a Si_3N_4 buffer layer, which was shown to be between 700 and 750 °C by tracking the emergence of bright peaks in the RHEED pattern[29]. Other work has observed the crystallization of pure ALD deposited hafnium oxide films with x-ray methods, in which case thickness-dependent crystallization occurred between 425 °C (40 nm films) and 600 °C (5 nm films) for films deposited via ALD at 300 °C[45]. The increased crystallization temperature relative to pure HfO_2 was likely due to the incorporation of Al in the film. We note that in this work, a streaky RHEED pattern was observed, whereas in the present study, diffuse rings were observed. This difference could be attributed to differences in final sample temperature, differences in film composition (Al-doped vs pure HfO_2), and/or differences in surface roughness. Nonetheless, our work and this prior work both demonstrate that crystallization of polycrystalline oxide ALD films can be monitored using RHEED.

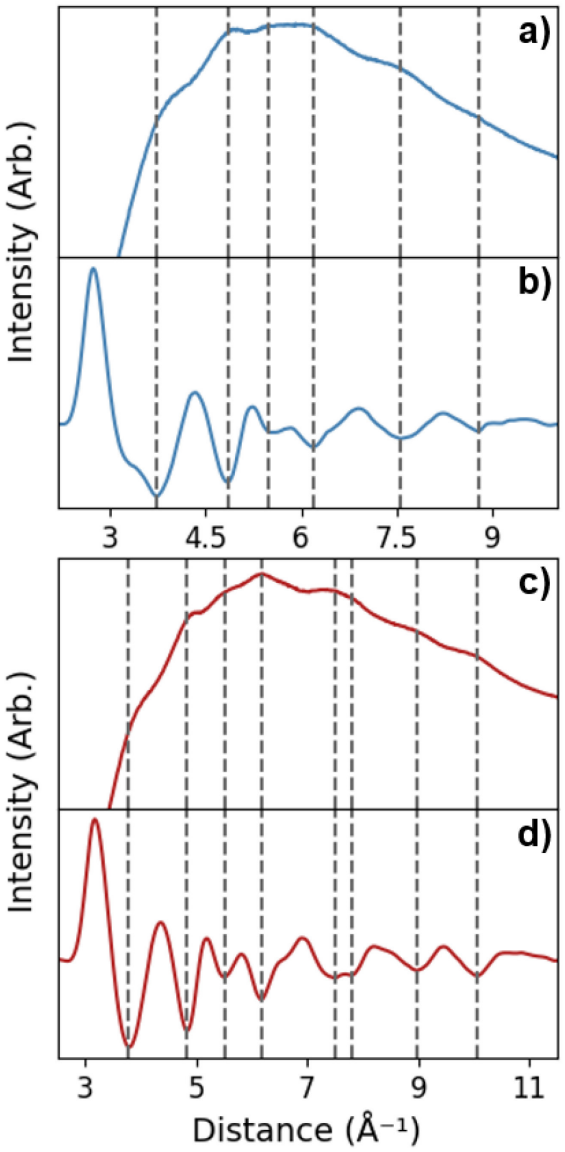

Figure 10: Radially integrated RHEED patterns of the 30 nm hafnia film after crystallization: a) raw data collected at 20 keV and b) second derivative, c) raw data at 15 keV, d) second derivative.

The trough positions in the second derivatives of the radially integrated RHEED images at 65 °C after heating were used to index the electron diffraction pattern. These positions are marked as the dotted lines in Figure 8a and 8b. As the higher index (hkl) peaks seen at 30 keV for a monoclinic structure tend to overlap and provide difficulty when indexing, RHEED data were also collected at 20 and 15 keV to reveal more easily identified lower (hkl) indexes (**Figure 10**). Similar to the 30 keV pattern, the second

derivatives of the radially integrated intensity were analyzed from images collected at 20 and 15 keV lines represent the peak positions (see Figure 10b and 10d).

d-spacing 15 keV	d-spacing 20 keV	d-spacing 30 keV	Proposed (hkl)	d-spacing proposed (hkl)	Peak Intensity
1.68			[1,2,2]	1.67	13.4
	1.66		[2,2,1]/[0,1,3]	1.66/1.65	13.0/0.3
	1.30		[-2,3,2]/[2,1,3]	1.30	6.6
1.29			[0,4,0]	1.30	3.3
1.14	1.14		[-3,3,2]/[-2,4,1]	1.15/1.14	4.5
1.02	1.02		[-4,2,3]/[0,5,1]/[1,5,0]	1.02	3.1/3.1/1.6
		0.96	[3,0,4]/[0,5,2]	0.97/0.96	2.6
	0.84		[1,0,6]/[4,3,3]/[-3,3,5]	0.84	1.6
0.83			[-6,1,2]/[-4,2,5]	0.83	1.6
	0.81	0.81	[4,2,4]/[6,1,1]/[-4,5,1]	0.81	1.4
0.72			[2,3,6]/[1,1,7]	0.72	0.9
	0.70		[1,7,2]/[3,4,5]/[-7,2,2]	0.70	0.9
		0.69	[5,4,3]/[-2,7,2]	0.70/0.69	0.8
	0.62		[-6,4,5]/[-7,2,5]	0.62	0.6

Table 1: Indexed peaks from the second derivatives of the radially integrated RHEED images from Figure 7 and 10 along with their relative electron intensities.

The trough positions were used as the $R_{(hkl)}$ in Equation 3 with the known camera length (L) to determine the possible, specific (hkl) parent planes (Table 1). The d spacings calculated from the RHEED images coincide well with some of the calculated electron diffraction d spacings from monoclinic hafnia. The monoclinic crystal structure has many characteristic rings that can be difficult to distinguish. Identifying distinct rings is more complicated because the deposited film has a nanocrystalline structure which causes the rings to appear diffuse. This is in contrast to the sharp, well-defined rings from a RHEED pattern observed for a monoclinic HfO_2 film deposited at high temperature[46]. The diffuse rings may blend together, which can cause some rings to be identified in the 15 or 20 keV and not in the 30 keV diffraction pattern. Since some ring d spacings only vary by 0.01, it can be challenging to properly index ring d spacings to specific (hkl) and to determine which distinct rings are present or which sets of rings are blended together. Therefore, distinct groups of planes were assigned and grouped to match the measured

positions as best as possible in this work. The presence of monoclinic HfO_2 in our samples was confirmed using, *ex situ* XRD (Supplemental Figure 4).

Conclusion

This paper presented the design, assembly, and testing of an ALD chamber with RHEED capabilities. We detailed the requirements and best practices for incorporating RHEED into a custom chamber with the capability to perform both high vacuum *in situ* characterization of a film between deposition cycles and low vacuum *in situ* monitoring in real time of a depositing ALD film with the addition of a re-entrant RHEED screen and an additional pumping zone between the chamber and electron source. Although we did not demonstrate RHEED *during* ALD pulses (the DDP configuration) due to financial and time constraints on the work, we have outlined the required hardware and pressure requirements as well as the advantages (higher P operation) of this measurement configuration.

This custom ALD chamber was calibrated using a polycrystalline gold sample. To confirm the accuracy of the calibration, an ALD hafnia film was deposited on Si and its crystallization temperature and resulting structure was observed with RHEED. Analysis of the RHEED images confirmed that the hafnia film crystallized in the expected monoclinic structure with experimentally determined d spacings agreeing with those calculated using ideal crystal parameters.

An ALD chamber with electron diffraction capabilities may allow for the nuanced structural transformations to be observed in real time. For ALD films with many polymorphs, factors such as deposition chemistry and conditions, annealing time and temperature, substrate crystal structure, and ambient gas composition can influence the resulting film structure. *In situ* observation of the structural changes resulting from varying these factors is vital to understanding the growth process and controlling structure and properties. This technique can also provide understanding of what process parameters impact the crystallization of many high-temperature oxides and how changing these parameters directly affects

the resulting structure. The ability to fine-tune the crystal structure of oxides that were previously only able to be deposited as amorphous films would allow for their incorporation into the active layers of electronics and other applications that require fine-tuned crystallinity or epitaxy. This understanding will provide vital information that will influence the design of future technology.

Supplementary Material

Supplemenatary materials are available online including a detailed parts list, system photographs, RHEED data, and XRD data.

TOC Figure

Acknowledgements

This work was funded by the National Science Foundation Division for Materials Research CAREER Award #1752956.

Author Declarations

Conflict of Interest

The authors have no conflicts to disclose.

Author Contributions

A. Howzen: Formal analysis (lead), Investigation (lead), Methodology (lead), Software (lead), Writing—original draft (lead), Writing—review and editing (equal), **J. Caspar**: Formal analysis (equal), Software (equal), Writing—review and editing (equal), **A. Oztekin**: Supervision (equal), Writing—review and editing (equal), and **N. Strandwitz**: Conceptualization (lead), Funding acquisition (lead), Project administration (lead), Resources (lead), Supervision (lead), Writing—review and editing (equal).

References:

(1) George, S. M. Atomic Layer Deposition: An Overview. *Chem Rev* **2010**, *110* (1), 111–131. https://doi.org/10.1021/cr900056b.

(2) Ritala, M.; Kukli, K.; Rahtu, † Antti; Räisänen, P. I.; Leskelä, M.; Sajavaara, T.; Keinonen, J. Atomic Layer Deposition of Oxide Thin Films with Metal Alkoxides as Oxygen Sources. *Science (1979)* **2000**, *288*, 319–321.

(3) Foroughi-Abari, A.; Cadien, K. Atomic Layer Deposition for Nanotechnology. In *Nanofabrication*; Springer Vienna: Vienna, 2012; pp 143–161. https://doi.org/10.1007/978-3-7091-0424-8_6.

(4) Miikkulainen, V.; Leskelä, M.; Ritala, M.; Puurunen, R. L. Crystallinity of Inorganic Films Grown by Atomic Layer Deposition: Overview and General Trends. *Journal of Applied Physics*. January 14, 2013. https://doi.org/10.1063/1.4757907.

(5) Vasić, R.; Consiglio, S.; Clark, R. D.; Tapily, K.; Sallis, S.; Chen, B.; Newby, D.; Medikonda, M.; Raja Muthinti, G.; Bersch, E.; Jordan-Sweet, J.; Lavoie, C.; Leusink, G. J.; Diebold, A. C. Multi-Technique x-Ray and Optical Characterization of Crystalline Phase, Texture, and Electronic Structure of Atomic Layer Deposited Hf1−xZrxO2 Gate Dielectrics Deposited by a Cyclical Deposition and Annealing Scheme. *J Appl Phys* **2013**, *113* (23). https://doi.org/10.1063/1.4811446.

(6) Bhuyian, M.; Misra, D.; Tapily, K.; Clark, R.; Consiglio, S.; Wajda, C.; Nakamura, G.; Leusink, G. Reliability of ALD $Hf_{1-X}Zr_xO_2$ Deposited by Intermediate Annealing or Intermediate Plasma Treatment. *ECS Trans* **2013**, *58* (7), 17–29. https://doi.org/10.1149/05807.0017ecst.

(7) Clark, R. D.; Consiglio, S.; Nakamura, G.; Trickett, Y.; Leusink, G. J. Optimizing ALD HfO_2 for Advanced Gate Stacks with Interspersed UV and Thermal Treatments- DADA and MDMA Variations, Combinations, and Optimization. *ECS Trans* **2011**, *41* (2), 79–88. https://doi.org/10.1149/1.3633657.

(8) Conley, J. F.; Ono, Y.; Tweet, D. J. Densification and Improved Electrical Properties of Pulse-Deposited Films via *in Situ* Modulated Temperature Annealing. *Appl Phys Lett* **2004**, *84* (11), 1913–1915. https://doi.org/10.1063/1.1667619.

(9) Conley, J. F.; Tweet, D. J.; Ono, Y.; Stecker, G. Interval Annealing During Alternating Pulse Deposition. *MRS Proceedings* **2004**, *811*, D1.3. https://doi.org/10.1557/PROC-811-D1.3.

(10) Henke, T.; Knaut, M.; Hossbach, C.; Geidel, M.; Albert, M.; Bartha, J. W. Growth of Aluminum Oxide Thin Films with Enhanced Film Density by the Integration of in Situ Flash Annealing into Low-Temperature Atomic Layer Deposition. *Surf Coat Technol* **2017**, *309*, 600–608. https://doi.org/10.1016/j.surfcoat.2016.11.048.

(11) Henke, T.; Knaut, M.; Hossbach, C.; Geidel, M.; Rebohle, L.; Albert, M.; Skorupa, W.; Bartha, J. W. Flash-Lamp-Enhanced Atomic Layer Deposition of Thin Films. *ECS Trans* **2014**, *64* (9), 167–189. https://doi.org/10.1149/06409.0167ecst.

(12) Henke, T.; Knaut, M.; Hossbach, C.; Geidel, M.; Rebohle, L.; Albert, M.; Skorupa, W.; Bartha, J. W. Flash-Enhanced Atomic Layer Deposition: Basics, Opportunities, Review, and Principal Studies on the Flash-Enhanced Growth of Thin Films. *ECS Journal of Solid State Science and Technology* **2015**, *4* (7), P277–P287. https://doi.org/10.1149/2.0301507jss.

(13) Piercy, B. D.; Wooding, J. P.; Gregory, S. A.; Losego, M. D. Pulsed Heating Atomic Layer Deposition (PH-ALD) for Epitaxial Growth of Zinc Oxide Thin Films on *c* -Plane Sapphire. *Dalton Transactions* **2022**, *51* (1), 303–311. https://doi.org/10.1039/D1DT03581A.

(14) Dendooven, J.; Solano, E.; Minjauw, M. M.; Van de Kerckhove, K.; Coati, A.; Fonda, E.; Portale, G.; Garreau, Y.; Detavernier, C. Mobile Setup for Synchrotron Based *in Situ* Characterization during Thermal and Plasma-Enhanced Atomic Layer Deposition. *Review of Scientific Instruments* **2016**, *87* (11). https://doi.org/10.1063/1.4967711.

(15) Devloo-Casier, K.; Dendooven, J.; Ludwig, K. F.; Lekens, G.; D'Haen, J.; Detavernier, C. *In Situ* Synchrotron Based x-Ray Fluorescence and Scattering Measurements during Atomic Layer Deposition: Initial Growth of HfO2 on Si and Ge Substrates. *Appl Phys Lett* **2011**, *98* (23). https://doi.org/10.1063/1.3598433.

(16) Nepal, N.; Anderson, V. R.; Johnson, S. D.; Downey, B. P.; Meyer, D. J.; DeMasi, A.; Robinson, Z. R.; Ludwig, K. F.; Eddy, C. R. Real-Time Growth Study of Plasma Assisted Atomic Layer Epitaxy of InN Films by Synchrotron x-Ray Methods. *Journal of Vacuum Science & Technology A: Vacuum, Surfaces, and Films* **2017**, *35* (3). https://doi.org/10.1116/1.4978026.

(17) Boichot, R.; Tian, L.; Richard, M.-I.; Crisci, A.; Chaker, A.; Cantelli, V.; Coindeau, S.; Lay, S.; Ouled, T.; Guichet, C.; Chu, M. H.; Aubert, N.; Ciatto, G.; Blanquet, E.; Thomas, O.; Deschanvres, J.-L.; Fong, D. D.; Renevier, H. Evolution of Crystal Structure During the Initial Stages of ZnO Atomic Layer Deposition. *Chemistry of Materials* **2016**, *28* (2), 592–600. https://doi.org/10.1021/acs.chemmater.5b04223.

(18) Methaapanon, R.; Geyer, S. M.; Brennan, S.; Bent, S. F. Size Dependent Effects in Nucleation of Ru and Ru Oxide Thin Films by Atomic Layer Deposition Measured by Synchrotron Radiation X-Ray Diffraction. *Chemistry of Materials* **2013**, *25* (17), 3458–3463. https://doi.org/10.1021/cm401585k.

(19) Hur, T.-B.; Hwang, Y.-H.; Kim, H.-K.; Park, H.-L. Study of the Structural Evolution in ZnO Thin Film by *in Situ* Synchrotron x-Ray Scattering. *J Appl Phys* **2004**, *96* (3), 1740–1742. https://doi.org/10.1063/1.1762706.

(20) Fong, D. D.; Eastman, J. A.; Kim, S. K.; Fister, T. T.; Highland, M. J.; Baldo, P. M.; Fuoss, P. H. *In Situ* Synchrotron x-Ray Characterization of ZnO Atomic Layer Deposition. *Appl Phys Lett* **2010**, *97* (19). https://doi.org/10.1063/1.3514254.

(21) Lee, H.-B.-R.; Park, Y. J.; Baik, S.; Kim, H. Initial Stage Growth during Plasma-Enhanced Atomic Layer Deposition of Cobalt. *Chemical Vapor Deposition* **2012**, *18* (1–3), 41–45. https://doi.org/10.1002/cvde.201106937.

(22) Klug, J. A.; Weimer, M. S.; Emery, J. D.; Yanguas-Gil, A.; Seifert, S.; Schlepütz, C. M.; Martinson, A. B. F.; Elam, J. W.; Hock, A. S.; Proslier, T. A Modular Reactor Design for *in Situ* Synchrotron x-Ray Investigation of Atomic Layer Deposition Processes. *Review of Scientific Instruments* **2015**, *86* (11). https://doi.org/10.1063/1.4934807.

(23) Geyer, S. M.; Methaapanon, R.; Johnson, R. W.; Kim, W.-H.; Van Campen, D. G.; Metha, A.; Bent, S. F. An Atomic Layer Deposition Chamber for *in Situ* x-Ray Diffraction and Scattering Analysis. *Review of Scientific Instruments* **2014**, *85* (5). https://doi.org/10.1063/1.4876484.

(24) Geyer, S. M.; Methaapanon, R.; Johnson, R.; Brennan, S.; Toney, M. F.; Clemens, B.; Bent, S. Structural Evolution of Platinum Thin Films Grown by Atomic Layer Deposition. *J Appl Phys* **2014**, *116* (6). https://doi.org/10.1063/1.4892104.

(25) Kuninori, K.; Masashi, O.; Kazuo, N. Reflection High-Energy Electron Diffraction of Heteroepitaxy in Chemical Vapor Deposition Reactor: Atomic-Layer Epitaxy of GaAs, AlAs and GaP on Si. *Jpn J Appl Phys* **1993**, *32* (3), 1051–1055.

(26) Yao, T. Dynamic Reflection High-Energy Electron Diffraction Observations of the Atomic Layer Epitaxy Growth of Zn Chaleogenides. *Jpn J Appl Phys* **1986**, *25* (12A), L942. https://doi.org/10.1143/JJAP.25.L942.

(27) Zhu, Z.; Hagino, M.; Uesugi, K.; Kamiyama, S.; Fujimoto, M.; Yao, T. Surface Processes in ALE and MBE Growth of ZnSe: Correlation of RHEED Intensity Variation with Surface Coverage. *Jpn J Appl Phys* **1989**, *28* (9R), 1659. https://doi.org/10.1143/JJAP.28.1659.

(28) Hu, S.; Lin, E. L.; Hamze, A. K.; Posadas, A.; Wu, H.; Smith, D. J.; Demkov, A. A.; Ekerdt, J. G. Zintl Layer Formation during Perovskite Atomic Layer Deposition on Ge (001). *J Chem Phys* **2017**, *146* (5). https://doi.org/10.1063/1.4972071.

(29) Park, J. W.; Kim, S. J. Reflective High-Energy Electron Diffraction Investigation of the Crystallization of Ultra-Thin Oxides. *Journal of the Korean Physical Society* **2005**, *47* (2), L182–L184. https://doi.org/10.3938/jkps.47.182.

(30) Ngo, T. Q.; Goble, N. J.; Posadas, A.; Kormondy, K. J.; Lu, S.; McDaniel, M. D.; Jordan-Sweet, J.; Smith, D. J.; Gao, X. P. A.; Demkov, A. A.; Ekerdt, J. G. Quasi-Two-Dimensional Electron Gas at the Interface of γ-Al2O3/SrTiO3 Heterostructures Grown by Atomic Layer Deposition. *J Appl Phys* **2015**, *118* (11). https://doi.org/10.1063/1.4930575.

(31) Chen, P.-Y.; Posadas, A. B.; Kwon, S.; Wang, Q.; Kim, M. J.; Demkov, A. A.; Ekerdt, J. G. Cubic Crystalline Erbium Oxide Growth on GaN(0001) by Atomic Layer Deposition. *J Appl Phys* **2017**, *122* (21). https://doi.org/10.1063/1.4999342.

(32) McDaniel, M. D.; Hu, C.; Lu, S.; Ngo, T. Q.; Posadas, A.; Jiang, A.; Smith, D. J.; Yu, E. T.; Demkov, A. A.; Ekerdt, J. G. Atomic Layer Deposition of Crystalline SrHfO3 Directly on Ge (001) for High- *k* Dielectric Applications. *J Appl Phys* **2015**, *117* (5). https://doi.org/10.1063/1.4906953.

(33) Lin, E. L.; Posadas, A. B.; Zheng, L.; Elliott Ortmann, J.; Abel, S.; Fompeyrine, J.; Lai, K.; Demkov, A. A.; Ekerdt, J. G. Atomic Layer Deposition of Epitaxial Ferroelectric Barium Titanate on Si(001) for Electronic and Photonic Applications. *J Appl Phys* **2019**, *126* (6). https://doi.org/10.1063/1.5087571.

(34) Le, T. T.; Lam, C. H.; Posadas, A. B.; Demkov, A. A.; Ekerdt, J. G. Epitaxial Growth by Atomic Layer Deposition and Properties of High- *k* Barium Strontium Titanate on Zintl-Templated Ge (001) Substrates. *Journal of Vacuum Science & Technology A* **2022**, *40* (1). https://doi.org/10.1116/6.0001445.

(35) Bankras, R. G. In-Situ RHEED and Characterization of ALD Al2O3 Gate Dielectrics. Dissertation, University of Twente.

(36) Bankras, R.; Holleman, J.; Schmitz, J.; Sturm, M.; Zinine, A.; Wormeester, H.; Poelsema, B. In Situ Reflective High-Energy Electron Diffraction Analysis During the Initial Stage of a Trimethylaluminum/Water ALD Process. *Chemical Vapor Deposition* **2006**, *12* (5), 275–279. https://doi.org/10.1002/cvde.200506433.

(37) Ichimiya, A.; Cohen, P. I. *Reflection High-Energy Electron Diffraction*; Cambridge University Press, 2004. https://doi.org/10.1017/CBO9780511735097.

(38) Smith, D. L. Mean Free Path. In *Thin Film Deposition: Principles and Practice*; McGraw-Hill: Boston, 1995; pp 23–25.

(39) Elam, J. W.; Groner, M. D.; George, S. M. Viscous Flow Reactor with Quartz Crystal Microbalance for Thin Film Growth by Atomic Layer Deposition. *Review of Scientific Instruments* **2002**, *73* (8), 2981. https://doi.org/10.1063/1.1490410.

(40) Singh, S.; Singh, D.; Singh, M. Synthesis of Nanostructured Thin Films for Resolution and Diffraction/ Camera Length Calibration of Transmission Electron Microscopes. *Indian Journal of Pure & Applied Physics* **2018**, *57*, 157–165.

(41) Zei, M. S.; Nakai, Y.; Lehmpfuhl, G.; Kolb, D. M. The Structure of Gold and Silver Films Evaporated on Glass: A Leed and Rheed Study. *J Electroanal Chem Interfacial Electrochem* **1983**, *150* (1–2), 201–208. https://doi.org/10.1016/S0022-0728(83)80202-2.

(42) Zhang, X.-Y.; Hsu, C.-H.; Lien, S.-Y.; Wu, W.-Y.; Ou, S.-L.; Chen, S.-Y.; Huang, W.; Zhu, W.-Z.; Xiong, F.-B.; Zhang, S. Temperature-Dependent HfO2/Si Interface Structural Evolution and Its Mechanism. *Nanoscale Res Lett* **2019**, *14* (83). https://doi.org/10.1186/s11671-019-2915-0.

(43) Zhang, X.-Y.; Han, J.; Peng, D.-C.; Ruan, Y.-J.; Wu, W.-Y.; Wuu, D.-S.; Huang, C.-J.; Lien, S.-Y.; Zhu, W.-Z. Crystallinity Effect on Electrical Properties of PEALD–HfO2 Thin Films Prepared by Different Substrate Temperatures. *Nanomaterials (Basel)* **2022**, *12* (21). https://doi.org/10.3390/nano12213890.

(44) Win, T. S.; Kuzemenko, A. P.; Rodionov, V. V.; Than, M. M. Effect of the Annealing Temperature on the Structural Properties of Hafnium Nanofilms by Magnetron Sputtering. *J Phys Conf Ser* **2021**, *2064*, 1–7. https://doi.org/10.1088/1742-6596/2064/1/012071.

(45) Gusev, E. P.; Cabral, C.; Copel, M.; D'Emic, C.; Gribelyuk, M. Ultrathin HfO2 Films Grown on Silicon by Atomic Layer Deposition for Advanced Gate Dielectrics Applications. *Microelectron Eng* **2003**, *69* (2–4), 145–151. https://doi.org/10.1016/S0167-9317(03)00291-0.

(46) Aarik, J.; Aidla, A.; Mändar, H.; Uustare, T.; Kukli, K.; Schuisky, M. Phase Transformations in Hafnium Dioxide Thin Films Grown by Atomic Layer Deposition at High Temperatures. *Appl Surf Sci* **2001**, *173* (1–2), 15–21. https://doi.org/10.1016/S0169-4332(00)00859-X.